Yu *et al. Chem Synth* 2023;3:3
DOI: 10.20517/cs.2022.30

Chemical Synthesis

Research Article

Open Access

Check for updates

Photothermal catalytic H_2 production over hierarchical porous $CaTiO_3$ with plasmonic gold nanoparticles

Xinti Yu[1,#], Zechuan Yu[2,#], Heng Zhao[1], Ian D. Gates[1], Jinguang Hu[1,*]

[1]Department of Chemical and Petroleum Engineering, University of Calgary, Calgary T2N 1N4, Canada.
[2]School of Civil Engineering and Architecture, Wuhan University of Technology, Wuhan 430070, Hubei, China.
[#]Both Authors contributed equally.

[*]**Correspondence to:** Prof. Jinguang Hu, Department of Chemical and Petroleum Engineering, University of Calgary, 2500 University Drive NW, Calgary T2N 1N4, Canada. E-mail: jinguang.hu@ucalgary.ca

How to cite this article: Yu X, Yu Z, Zhao H, Gates ID, Hu J. Photothermal catalytic H_2 production over hierarchical porous $CaTiO_3$ with plasmonic gold nanoparticles. *Chem Synth* 2023;3:3. https://dx.doi.org/10.20517/cs.2022.30

Received: 3 Oct 2022 **First Decision:** 6 Dec 2022 **Revised:** 19 Dec 2022 **Accepted:** 28 Dec 2022 **Published:** 6 Jan 2023

Academic Editors: Bao-Lian Su, Da-Gang Yu **Copy Editor:** Ke-Cui Yang **Production Editor:** Ke-Cui Yang

Abstract

The synergistic promotion by photocatalysis and thermocatalysis is a promising approach for sustainable hydrogen (H_2) production. Herein, we rationally design a perovskite-based catalyst with three-dimensionally ordered macroporous structure (3DOM $CaTiO_3$-Au) for photothermal catalytic H_2 production from different substrates. The hierarchical 3DOM structure facilitates light harvesting and mass diffusion of the substrates, while the gold nanoparticles (Au NPs) promote charge separation. The photogenerated and hot electrons are oriented accumulated on the surface of Au NPs. The non-metallic gold species [Au(I)] show more activity for H_2 evolution. As a result, 3DOM $CaTiO_3$-Au exhibits excellent activity for H_2 production from glycerol and other substrates with hydroxyl groups. The present work demonstrates a feasible approach to improve sustainable H_2 production by rationally designing and fabricating efficient photothermal catalysts.

Keywords: 3DOM $CaTiO_3$, plasmonic Au NPs, photothermal catalysis, H_2 production, mechanism investigation

INTRODUCTION

Hydrogen (H_2), a clean and sustainable energy vector, has been widely recognized as a promising alternative to traditional fossil fuels[1]. Currently, about 96% of H_2 is produced from the steam reforming process, which

requires a huge amount of energy input and results in CO_2 emission[2]. Comparably, solar-driven water splitting is a more energy-saving and sustainable approach for H_2 generation[3-8]. However, the present water splitting activity has been greatly limited by the energetically and kinetically demanding process of O_2 evolution reaction (OER)[9,10]. In the present work, numerous investigations have been conducted to replace the OER with organic photo-oxidation, which could not only reduce the energy demand for H_2 generation but also provide an alternative to simultaneously produce value-added chemicals[11-17].

To realize the above scenario, the rational design of dual-functional photocatalysts is highly desired. The excellent candidate should have multiple abilities in light harvesting, enhanced charge separation and favorable surface reaction kinetics[18,19]. In terms of light harvesting, the hierarchically porous structure stands out due to the multiple scattering effect, prolonging the interaction between incident photons with photocatalytic materials[20-22]. Three-dimensionally ordered macroporous (3DOM) structure has been extensively applied in photocatalytic applications because of its outstanding competence in improving light absorption and facilitating mass diffusion[23-26]. Our previous investigation has revealed the significant promotion in photocatalytic H_2 production by $CaTiO_3$ perovskite with 3DOM structure and carbon quantum dots as cocatalysts, which exhibited comparable activity as 3DOM $CaTiO_3$-Au[27]. Considering the excellent photo- and thermal effects of perovskite and gold nanoparticles, it could be foreseen that H_2 production activity would be significantly boosted with the synergistic promotion by photocatalysis and thermocatalysis[28,29].

Limited by the high Gibbs free energy of most chemical reactions, the overall activity of most photocatalysis is still in the primary stage[30]. Herein, photothermal catalysis with the assistance of heating to improve the solar-to-hydrogen efficiency has begun to emerge in most recent years[31-33]. Metal nanomaterials with localized surface plasmon resonance (LSPR) effect have been widely utilized in photothermal applications, such as gold[34]. The widely recognized mechanism in this case is the photo-assisted thermocatalysis, in which the local temperature on these metal nanomaterials could be as high as > 70 °C under irradiation, thereby enhancing reaction kinetics[35]. However, the synergistic promotion of H_2 generation could only achieve 2-5 folders as the LSPR of these metal nanomaterials generates a limited number of active electrons, which would be partially transferred to the conduction band of the contacted semiconductors[36]. Due to the sluggish H_2 evolution reaction on the surface of semiconductor compared with metal materials, photo-assisted thermocatalysis still has significant scope for improvement. From this point of view, accumulating more electrons on the surface of plasmonic gold nanoparticles with extra heating from activated semiconductor materials is a feasible approach to further improve the activity of H_2 production. Besides, non-metallic gold species ($Au^{\delta+}$) have been reported to have improved activity for photocatalytic reactions[37]. The internal mechanism has not been systematically investigated.

In the present work, we demonstrate the synergistic catalysis of photocatalysis and thermocatalysis for H_2 production by conducting the experiment under light irradiation and at a controlled temperature. 3DOM $CaTiO_3$ is firstly synthesized by the colloid-template method and gold nanoparticles (Au NPs) are then loaded on the surface to obtain the photothermal catalyst. The as-prepared 3DOM $CaTiO_3$-Au exhibits hierarchically porous structure in long range and shows significant improvement in visible light absorption due to the LSPR effect. As a result, the 3DOM $CaTiO_3$-Au shows excellent H_2 production (145.2 μmol) from photothermal glycerol reforming, which is about 57 times and 13 times higher than that from thermocatalysis and photocatalysis, respectively. The oriented accumulation of photothermal electrons on the surface of Au NPs with oxidized species greatly reduces the energy barrier for hydrogen evolution. The present work demonstrates an example of boosting hydrogen production by coupling photocatalysis with thermocatalysis with the rational design of a catalyst.

RESULTS AND DISCUSSION

The fabrication process of 3DOM $CaTiO_3$-Au is illustrated in Figure 1A. Briefly, the obtained polystyrene spheres by the surfactant-free emulsion polymerization method are assembled into a colloid template. The precursor containing $Ca(NO_3)_2$ and titanium (IV) isopropoxide then fills the voids of the template, accompanied by the simultaneous hydrolysis reaction. After calcination in air with gradient programs, the 3DOM $CaTiO_3$ is obtained with $CaCO_3$ impurity on the surface. Finally, gold nanoparticles are loaded on the acid-washed 3DOM $CaTiO_3$ by sodium borohydride reduction method. As the quality of colloid template plays a vital role in the formation of 3DOM structure, the assembled polystyrene spheres are first characterized by scanning electron microscopy (SEM). The highly ordered assembly of polystyrene spheres is revealed in Figure 1B. Figure 1C displays the low-resolution SEM image of the fabricated 3DOM $CaTiO_3$ which is an assembly of relatively uniform three-dimensionally ordered macroporous structure. The framework of 3DOM $CaTiO_3$ is constructed by porous nanosheet, which has been well explained in our previous investigation [Figure 1D]. Transmission electron microscopy (TEM) images at low resolution also reveal the hierarchically porous structure with well-distributed gold nanoparticles [Figure 1E and F]. The statistical result of the gold nanoparticles shows a broad size distribution and they concentrate in 8 nm [Supplementary Figure 1]. The high crystallinity could be revealed by the distinguished lattices with a spacing of 0.27 nm, corresponding to the (112) crystal facet of orthorhombic $CaTiO_3$ [Figure 1G]. The element mappings reveal the uniform distribution of each element in the structure [Supplementary Figure 2].

Figure 2A shows the XRD patterns of the 3DOM $CaTiO_3$ and 3DOM $CaTiO_3$-Au. $CaTiO_3$ phase was confirmed by the comparison between the XRD patterns and the Joint Committee on Powder Diffraction Standards (JCPDS) card no. 01-078-1013. The as-fabricated $CaTiO_3$ has pure phase and good crystallinity. All diffraction peaks can be assigned to the orthorhombic structure. The inset in Figure 2A is the partial enlarged detail and the peak around 38.3° corresponds to the (111) lattice plane of Au, which reveals the presence of Au in $CaTiO_3$. The XRD patterns of the $CaTiO_3$ unwashed by diluted nitric acid are shown in Supplementary Figure 3. In addition to $CaTiO_3$, the impurity $CaCO_3$ was also observed. The Ca^{2+} outside the crystal structure of $CaTiO_3$ interacted with CO_2 to form $CaCO_3$ during the calcination process. The initial molar ratio of Ca and Ti was 1:1, and the formation of $CaCO_3$ indicated the presence of cation defects in the crystal structure[38].

The optical properties of 3DOM $CaTiO_3$ and 3DOM $CaTiO_3$-Au have been measured by UV-vis diffuse reflectance spectroscopy and the corresponding spectra are shown in Figure 2B. The optical band gap values obtained through the linear fitting of tails from the UV-vis spectra are shown in the inset of Figure 2B. All the samples are of the same size and thickness. The strong absorption at a wavelength range below 400 nm matches the intrinsic inter-band transition absorption of orthorhombic $CaTiO_3$[39]. As shown in the inset of Figure 2B, the band gap of as-fabricated 3DOM $CaTiO_3$ is approximately 3.25 eV, corresponding to an optical absorption edge of 382 nm. After the introduction of AuNPs, the light absorption is greatly improved. The broad peak at 540 nm of 3DOM $CaTiO_3$-Au composite corresponds to surface plasmon resonance (SPR) absorption of Au nanoparticles.

The chemical states on the surface of catalysts have been investigated by X-ray photoelectron spectroscopy (XPS), where characteristic peaks of Ca, Ti, O, Au and C are observed in the general survey scan [Supplementary Figure 4A]. All the XPS data has been calibrated by C 1s at 284.8 eV [Supplementary Figure 4B]. The pristine 3DOM $CaTiO_3$ and the modified composite of 3DOM $CaTiO_3$-Au show the unchanged binding energies of Ti 2p and O 1s [Supplementary Figure 4C and D]. However, a significant shift to lower binding energy in Ca 2p spectra is identified with the loading of Au NPs onto the

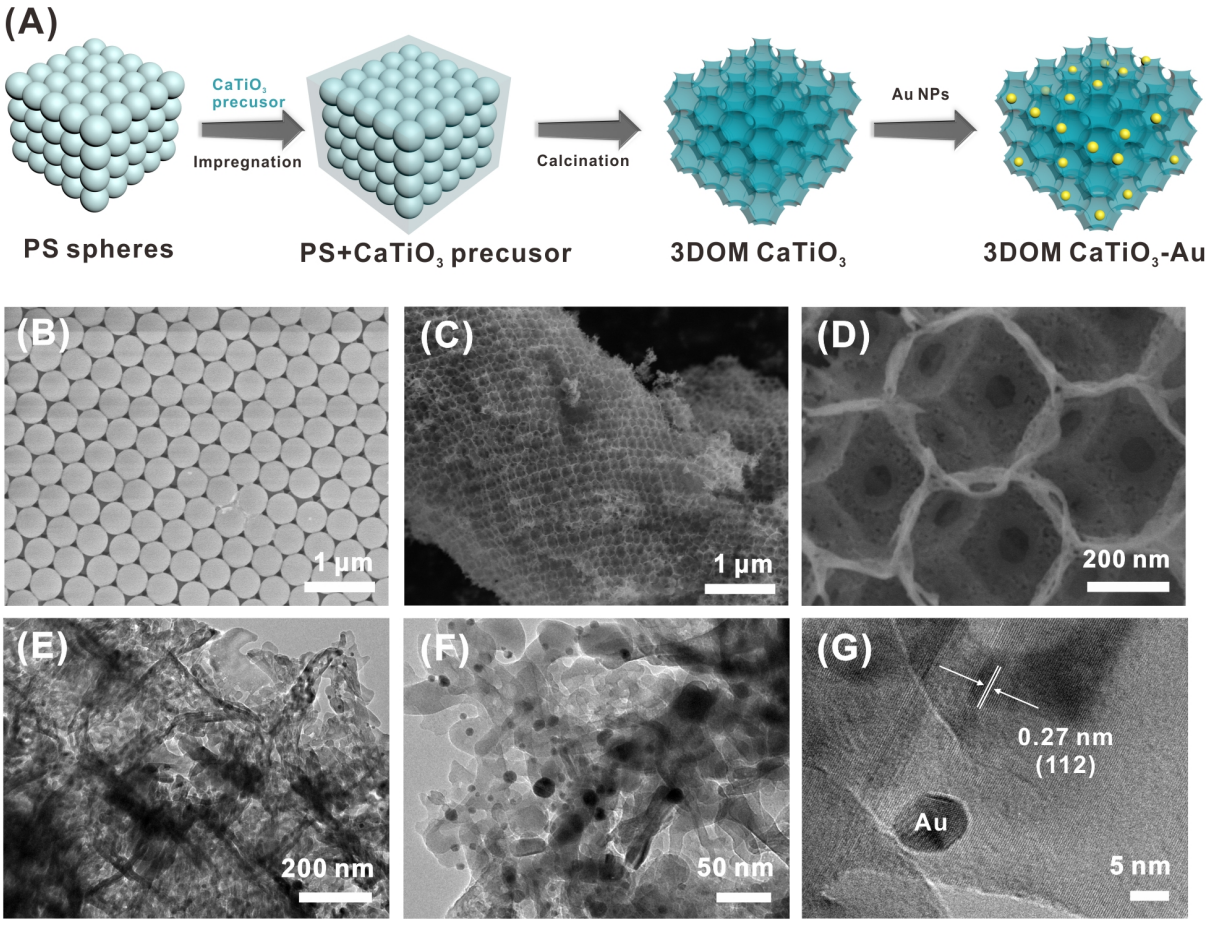

Figure 1. (A) Schematic illustration of the fabrication process of 3DOM $CaTiO_3$-Au, SEM images of (B) assembled polystyrene spheres; (C) 3DOM $CaTiO_3$ with low resolution; (D) 3DOM $CaTiO_3$ with high resolution; (E) and (F) Low-resolution TEM images of 3DOM $CaTiO_3$-Au; (G) high-resolution TEM image of 3DOM $CaTiO_3$-Au.

surface of $CaTiO_3$, indicating the spontaneous electron transfer due to the formation of Schottky junctions [Figure 2C][40]. More importantly, the oxidized species of gold is also identified apart from the metallic state, which is consistent with our previous investigation [Figure 2D][37]. The relative percentage of Au (I) is calculated to be around 3.2%. The detected Ti-OH in the O 1s spectra indicated the presence of oxygen vacancy in both 3DOM $CaTiO_3$ and 3DOM $CaTiO_3$-Au, which could be further revealed by the electron paramagnetic resonance (EPR) results [Supplementary Figure 5]. Noticeably, the intensity of oxygen vacancy increases with the introduction of gold nanoparticles, which may attribute to the high reduction ability of sodium borohydride.

The activity of as-prepared catalysts was evaluated by thermos-photocatalytic glycerol reforming for H_2 production. To reveal the synergistic promotion of thermocatalysis and photocatalysis, H_2 production over different catalysts was first investigated *via* thermocatalysis at 100 °C and photocatalysis, respectively. $CaTiO_3$ and 3DOM $CaTiO_3$ produce a similar amount of H_2 after 11 h reaction (0.47 μmol and 0.52 μmol respectively), indicating the negligible contribution of 3DOM structure in thermocatalytic H_2 production of pristine $CaTiO_3$ [Figure 3A]. With the loading of gold nanoparticles, the amount of H_2 significantly increases to 2.55 μmol after 11 h reaction, which is probably attributed to the mass diffusion property of hierarchical 3DOM structure. Another feature of 3DOM structure is light harvesting, which facilitates activating $CaTiO_3$ to produce more electrons and holes[41]. The promotion of H_2 production of 3DOM

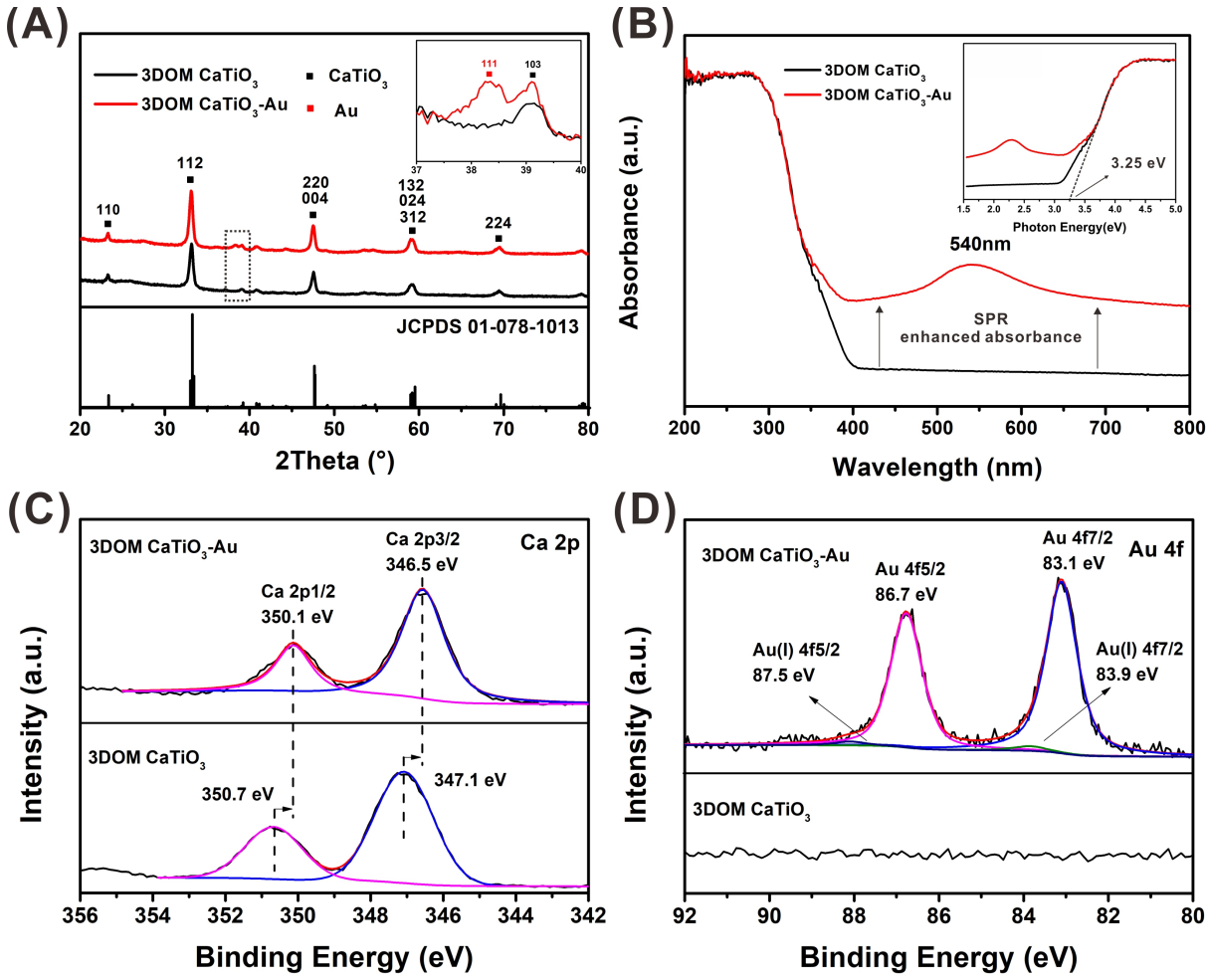

Figure 2. (A) XRD patterns; (B) UV-vis absorption spectra, high-resolution XPS spectra of (C) Ca 2p; and (D) Au 4f of 3DOM $CaTiO_3$ and 3DOM $CaTiO_3$-Au.

structure could be revealed by the performance of $CaTiO_3$ (0.26 μmol) and 3DOM $CaTiO_3$ (0.70 μmol) under the Xenon lamp irradiation [Figure 3B]. After loading gold nanoparticles, about 30 folders and 17 folders in H_2 production after 11 h reaction is achieved for $CaTiO_3$-Au (7.89 μmol) and 3DOM $CaTiO_3$-Au (11.67 μmol), respectively. The synergistic enhancement is further realized by coupling thermocatalysis at 100 °C and photocatalysis for all the four catalysts. The amount of H_2 generation at 11-h reaction for $CaTiO_3$, 3DOM $CaTiO_3$, $CaTiO_3$-Au and 3DOM $CaTiO_3$-Au is boosted to 18.91 μmol, 40.60 μmol, 90.41 μmol and 145.2 μmol, respectively [Figure 3C]. The comparison in H_2 production for each catalyst under different reaction conditions further demonstrates the significant promotion by photothermal approach [Supplementary Figures 6-9 and Supplementary Table 1]. Compared to bare photocatalysis and thermocatalysis, the H_2 generation over 3DOM $CaTiO_3$-Au by photothermal catalysis is enhanced by about 12 and 58 folders, respectively. The effect of gold loading on the thermo-photocatalytic H_2 production was further investigated by changing the volume of used $HAuCl_4$. The variation of gold loading is revealed to have a negligible effect on H_2 production for $CaTiO_3$-Au without 3DOM structure. While 3DOM $CaTiO_3$-Au exhibits significant relation with the gold loading and 205.9 μmol of H_2 is produced at the 11-h reaction when the actual loading of gold was 1.90 wt% [Figure 3D], which is more efficient compared to the $CaTiO_3$-based catalyst in literature [Supplementary Table 2]. The reaction temperature is

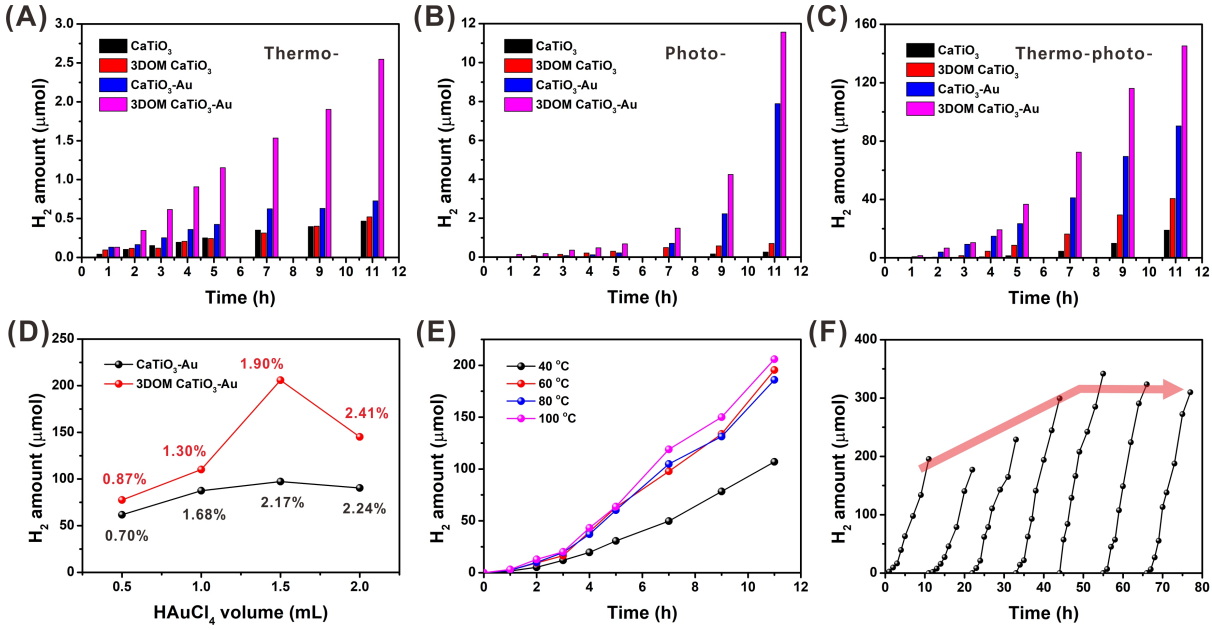

Figure 3. H_2 production over different catalysts *via* (A) thermocatalysis (100 °C); (B) photocatalysis; (C) thermo-photocatalysis (100 °C); (D) thermo-photocatalytic H_2 production over 3DOM $CaTiO_3$-Au prepared by different volumes of $HAuCl_4$ (actual loading of Au is labeled); (E) thermo-photocatalytic H_2 production over 3DOM $CaTiO_3$-Au prepared by 1.5 mL of $HAuCl_4$ under different reaction temperatures; and (F) long-time cycling test.

then changed to investigate its relationship with H_2 production [Figure 3E]. 3DOM $CaTiO_3$-Au exhibits similar activity when the temperature is above 60 °C, while the activity greatly reduces when the temperature is 40 °C. This indicates that 60 °C may be the threshold to fully activate 3DOM $CaTiO_3$-Au to produce active electrons for H_2 production. It should be mentioned that CO_2 was not observed during the reaction, indicating the absence of overoxidation. Some liquid products at extremely low concentrations were detected by high-performance liquid chromatography (HPLC) [Supplementary Figure 10]. However, the glycerol conversion was negligible (< 2%). The contribution of glycerol to H_2 production could be revealed by the control experiment in which pure water without glycerol is used as the reactant [Supplementary Figure 11]. It clearly shows that significant enhancement in H_2 production is achieved with the addition of glycerol, revealing the role of sacrificial agent of glycerol. The stability of 3DOM $CaTiO_3$-Au is tested at 60 °C during the long-time cycling reaction. In the first five cycles, 3DOM $CaTiO_3$-Au shows gradually increased activity and good stability could be revealed by the repeatability in H_2 production [Figure 3F].

To explain the internal reason for the gradual enhancement in H_2 production during the first five cycles, the used catalyst 3DOM $CaTiO_3$-Au was collected and characterized for its morphology and chemical state. The 3DOM structure in the long range is kept well after catalytic reaction and a little collapse could also be observed in the high-resolution SEM image [Figure 4A and B]. A significant change in the chemical state of gold is observed [Figure 4C]. Other elements have almost the same chemical state after catalytic reaction [Supplementary Figure 12]. The relative percentage of Au (I) increases from 3.2% to 8.7% after catalytic reaction. Electrostatic potential (ESP) difference is calculated by the addition of two oxygen atoms above the gold [Figure 4D]. The region near the binding site of proton overlaps the region with increased electrostatic potential, suggesting that the electron binding affected by the change in ESP would be relevant to chemical reactions involving hydrogen and electron. Contribution from the elevated ESP to the binding of an electron is 10 to 19 kcal/mol, which suggests a stronger electron binding capability of charged gold ions

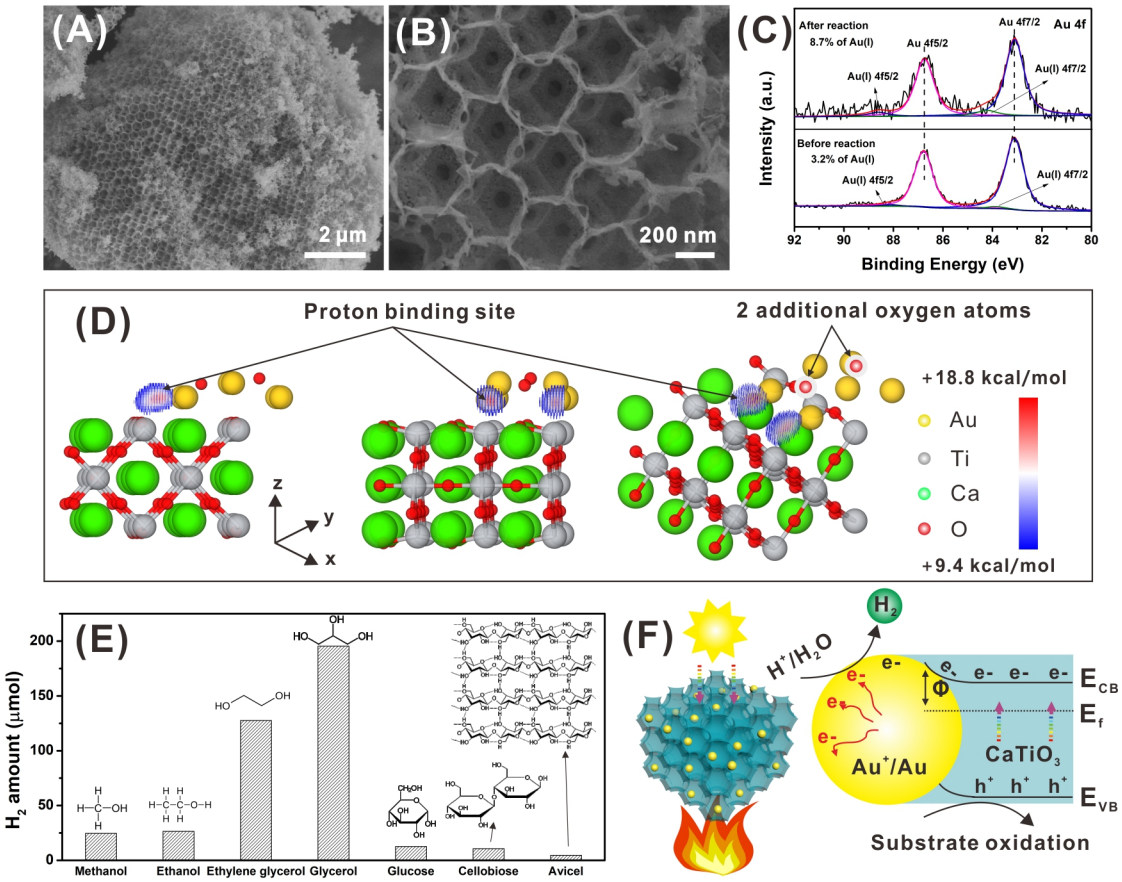

Figure 4. (A and B) SEM images of 3DOM $CaTiO_3$-Au after photocatalytic reaction; (C) XPS Au 4f spectra of 3DOM $CaTiO_3$-Au before and after photocatalytic reaction; (D) electrostatic potential difference brought by oxidization of gold atoms (the left and the middle are cross-section view of *yz* and *xz* plane, respectively. The right is a 3-D view of the electrostatic potential difference. The positive values indicate an elevated electrostatic potential by the addition of oxygen atoms); (E) H_2 production from different substrates; and (F) the proposed mechanism.

compared to the pristine gold atoms. Considering that the elevated ESP locates near the hydrogen binding site, we expect that the charged gold ions would exhibit a higher reactivity. The H_2 production from different substrates over 3DOM $CaTiO_3$-Au is also investigated. As the number of hydroxyl groups in the molecular structure from methanol to glycerol increases, the activity of H_2 production also increases [Figure 4E]. However, when the glucose and cellobiose with five and eight hydroxyl groups are used as the substrate, the H_2 production performance is greatly reduced, mainly due to the poor accessibility of these substrates with large dimensional structures to the catalyst[42,43]. Further inhibition of H_2 evolution is observed when cellulose with a more complex structure is used as the substrate. Therefore, the H_2 production performance is not only related to the number of hydroxyl groups but also the complexity of substrate structure. A brief mechanism is proposed herein [Figure 4F]. Under light irradiation, the electrons of $CaTiO_3$ are activated to conduction band, while the holes stay on the valence band. Due to the high work function of Au, the photogenerated electrons are then transferred to the surface of Au. With the assistance of extra heating, more electrons are accumulated from $CaTiO_3$ and the Au NPs also generate active hot electrons. All the electrons on the surface of Au NPs trigger the proton reduction reaction to produce H_2, while the substrate oxidation reaction is proceeded by the holes on the valence band.

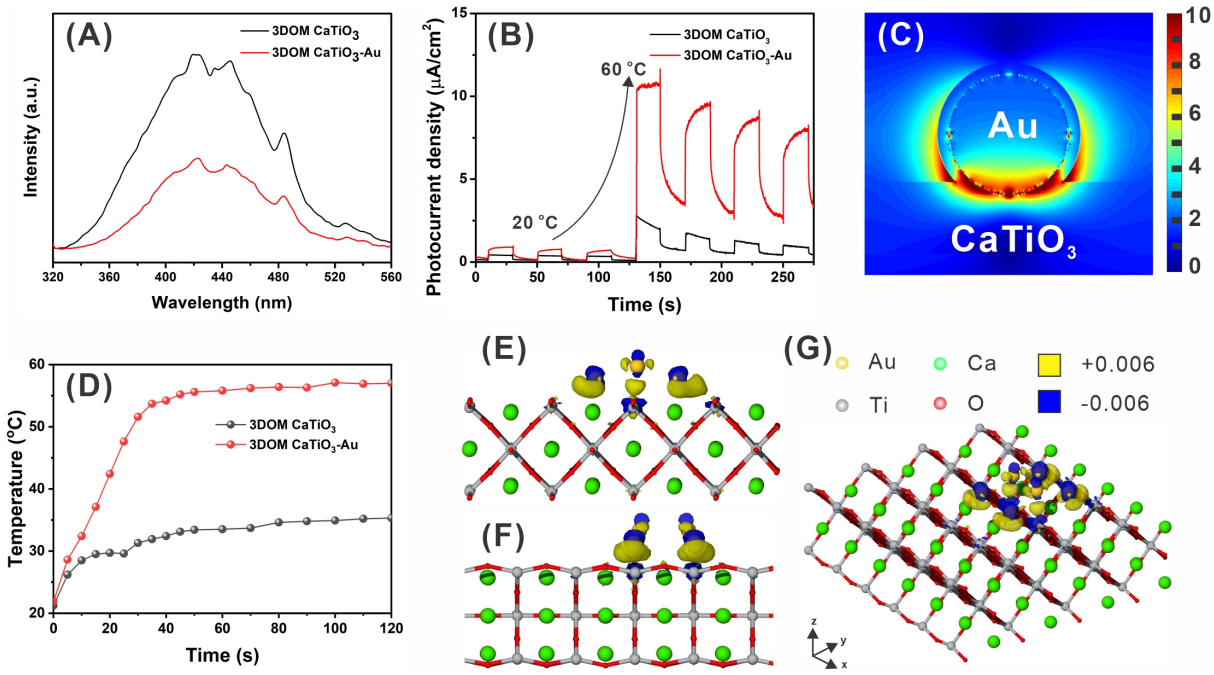

Figure 5. (A) PL; (B) photocurrent of 3DOM $CaTiO_3$ and 3DOM $CaTiO_3$-Au under different temperatures; (C) simulated electromagnetic field intensity distribution; (D) temperature of the catalyst with different light irradiation times for 3DOM $CaTiO_3$ and 3DOM $CaTiO_3$-Au. Isosurfaces of electronic density difference at the perovskite-gold interface from the cross-section view of (E) *yz* and (F) *xz* plane; (G) 3-D view of positive-value and negative-value isosurface in yellow and blue, respectively.

To reveal the improvement in charge separation after the introduction of Au NPs, steady photoluminescence (PL) spectra of 3DOM $CaTiO_3$ and 3DOM $CaTiO_3$-Au are collected with the excitation wavelength of 400 nm. 3DOM $CaTiO_3$-Au exhibits much reduced PL intensity, indicating the significant inhibition of photogenerated electrons and holes [Figure 5A]. To check the effect of temperature on the charge generation, transient photocurrent is measured. Both 3DOM $CaTiO_3$ and 3DOM $CaTiO_3$-Au show excellent responses to light irradiation [Figure 5B]. When the temperature of the electrolyte increases from 20 °C to 60 °C, more than 10 folders in photocurrent are achieved for 3DOM $CaTiO_3$-Au, revealing the generation of more electrons with the assistance of extra heating. To visually understand the charge separation, the electromagnetic field is simulated on a single Au nanoparticle [Figure 5C]. It is clear that the charge density on the surface of Au is much higher than that of $CaTiO_3$ and the highest electromagnetic field intensity is located at the interface of Au and $CaTiO_3$, indicating the formation of electron transfer channel at the interface and the immigration of active electrons from $CaTiO_3$ to Au. The photothermal effect of the catalyst is recorded by measuring the temperature of the 3DOM $CaTiO_3$ and 3DOM $CaTiO_3$-Au with different light irradiation times [Figure 5D]. Combined with the corresponding IR thermal images [Supplementary Figure 13,] it clearly shows the significant contribution to the photothermal effect by the gold nanoparticles. The electronic density difference brought by the addition of gold to perovskite is evaluated in real space and plotted [Figure 5E-G]. The isosurface in yellow encloses a space with enriched electronic density. We expect that this region favors proton binding. We place a hydrogen atom near the binding site and calculate that the total energy difference between the compound and individual components (the perovskite-gold model and a single hydrogen atom) is about -76.70 kcal/mol near gold and -93.48 kcal/mol near gold ions, which further indicates that oxidized gold species facilitate the H_2 evolution.

CONCLUSIONS

In summary, 3DOM $CaTiO_3$ is successfully fabricated by the colloid template method and Au NPs with partially oxidized species [Au(I)] are loaded to obtain 3DOM $CaTiO_3$-Au as the efficient catalyst for photothermal H_2 production. The 3DOM structure facilitates light harvesting and mass diffusion property, while the Au NPs help to improve the charge separation. As a result, 3DOM $CaTiO_3$-Au with optimized Au loading exhibits boosted activity for H_2 generation by the synergistic promotion of photocatalysis and thermocatalysis. Considerable H_2 is also achieved when the substrates are changed into biomass derivates. The oriented accumulation of electrons on the surface of Au NPs and the presence of Au(I) species are revealed to be the key factors. The present work provides a rational catalyst design to boost hydrogen production through synergistic photocatalysis and thermocatalysis.

DECLARATIONS

Authors' contributions

Made substantial contributions to conception and design of the study, performed data analysis and interpretation, and wrote the draft of manuscript: Yu X
Performed data acquisition and provided administrative, technical, and material support: Zhao H
Performed DFT calculation: Yu Z
Discussed and revised the manuscript: Gates ID, Hu J

Availability of data and materials

Detailed EXPERIMENTAL MATERIALS AND METHODS were published as Supplementary Materials in the journal. Other raw data that support the findings of this study are available from the corresponding author upon reasonable request.

Financial support and sponsorship

This work was finacially supported by the Canada First Research Excellence Fund (CFREF).

Conflicts of interest

All authors declared that there are no conflicts of interest.

Ethical approval and consent to participate

Not applicable.

Consent for publication

Not applicable.

REFERENCES

1. Majumdar A, Deutch JM, Prasher RS, Griffin TP. A framework for a hydrogen economy. *Joule* 2021;5:1905-8. DOI
2. Chen S, Pei C, Gong J. Insights into interface engineering in steam reforming reactions for hydrogen production. *Energy Environ Sci* 2019;12:3473-95. DOI
3. Wang Z, Li C, Domen K. Recent developments in heterogeneous photocatalysts for solar-driven overall water splitting. *Chem Soc Rev* 2019;48:2109-25. DOI PubMed
4. Thalluri SM, Bai L, Lv C, Huang Z, Hu X, Liu L. Strategies for semiconductor/electrocatalyst coupling toward solar-driven water splitting. *Adv Sci (Weinh)* 2020;7:1902102. DOI PubMed PMC
5. Wang Y, Vogel A, Sachs M, et al. Current understanding and challenges of solar-driven hydrogen generation using polymeric photocatalysts. *Nat Energy* 2019;4:746-60. DOI
6. Zhang P, Tian Z, Kang Y, et al. 10 nm Corrugated TiO_2 nanowire arrays by monomicelle-directed assembly for efficient hole extraction. *J Am Chem Soc* 2022;144:20964-74. DOI PubMed
7. Gao M, Zhang T, Ho GW. Advances of photothermal chemistry in photocatalysis, thermocatalysis, and synergetic

photothermocatalysis for solar-to-fuel generation. *Nano Res* 2022;15:9985-10005. DOI
8. Gao M, Peh CK, Zhu L, Yilmaz G, Ho GW. Photothermal catalytic gel featuring spectral and thermal management for parallel freshwater and hydrogen production. *Adv Energy Mater* 2020;10:2000925. DOI
9. Jamesh M, Harb M. Tuning the electronic structure of the earth-abundant electrocatalysts for oxygen evolution reaction (OER) to achieve efficient alkaline water splitting - a review. *J Energy Chem* 2021;56:299-342. DOI
10. Liu Y, Luo X, Zhou C, et al. A modulated electronic state strategy designed to integrate active HER and OER components as hybrid heterostructures for efficient overall water splitting. *Appl Catal B Environ* 2020;260:118197. DOI
11. Uekert T, Pichler CM, Schubert T, Reisner E. Solar-driven reforming of solid waste for a sustainable future. *Nat Sustain* 2021;4:383-91. DOI
12. Zhao H, Li CF, Liu LY, et al. n-p Heterojunction of TiO_2-NiO core-shell structure for efficient hydrogen generation and lignin photoreforming. *J Colloid Interf Sci* 2021;585:694-704. DOI PubMed
13. Zhao H, Li CF, Yong X, et al. Coproduction of hydrogen and lactic acid from glucose photocatalysis on band-engineered $Zn_{1-x}Cd_xS$ homojunction. *iScience* 2021;24:102109. DOI PubMed PMC
14. Nwosu U, Wang A, Palma B, et al. Selective biomass photoreforming for valuable chemicals and fuels: a critical review. *Renew Sust Energ Rev* 2021;148:111266. DOI
15. Wang J, Kumar P, Zhao H, Kibria MG, Hu J. Polymeric carbon nitride-based photocatalysts for photoreforming of biomass derivatives. *Green Chem* 2021;23:7435-57. DOI
16. Wu X, Luo N, Xie S, et al. Photocatalytic transformations of lignocellulosic biomass into chemicals. *Chem Soc Rev* 2020;49:6198-223. DOI PubMed
17. Li Y, Zhang D, Qiao W, et al. Nanostructured heterogeneous photocatalyst materials for green synthesis of valuable chemicals. *Chem Synth* 2022;2:9. DOI
18. Toe CY, Tsounis C, Zhang J, et al. Advancing photoreforming of organics: highlights on photocatalyst and system designs for selective oxidation reactions. *Energy Environ Sci* 2021;14:1140-75. DOI
19. Ma J, Liu K, Yang X, et al. Recent advances and challenges in photoreforming of biomass-derived feedstocks into hydrogen, biofuels, or chemicals by using functional carbon nitride photocatalysts. *ChemSusChem* 2021;14:4903-22. DOI
20. Chen LH, Li Y, Su BL. Hierarchy in materials for maximized efficiency. *Natl Sci Rev* 2020;7:1626-30. DOI PubMed PMC
21. Liu J, Zhao H, Wu M, et al. Slow photons for photocatalysis and photovoltaics. *Adv Mater* 2017;29:1605349. DOI PubMed
22. Baba T. Slow light in photonic crystals. *Nature Photon* 2008;2:465-73. DOI
23. Zhao H, Wu M, Liu J, Deng Z, Li Y, Su B. Synergistic promotion of solar-driven H_2 generation by three-dimensionally ordered macroporous structured TiO_2-Au-CdS ternary photocatalyst. *Appl Catal B Environ* 2016;184:182-90. DOI
24. Zhao H, Yu X, Hu G, et al. Confined synthesis of $BiVO_4$ nanodot and ZnO cluster co-decorated 3DOM TiO_2 for formic acid production from the xylan-based hemicellulose photorefinery. *Green Chem* 2021;23:8124-30. DOI
25. Zhao H, Li C, Yu X, et al. Mechanistic understanding of cellulose β-1,4-glycosidic cleavage via photocatalysis. *Appl Catal B Environ* 2022;302:120872. DOI
26. Liu J, Guo Y, Hu Z, et al. Slow photon-enhanced heterojunction accelerates photocatalytic hydrogen evolution reaction to unprecedented rates. *CCS Chem* 2022:1-13. DOI
27. Zhao H, Liu J, Li C, et al. Meso-microporous nanosheet-constructed 3dom perovskites for remarkable photocatalytic hydrogen production. *Adv Funct Mater* 2022;32:2112831. DOI
28. Mateo D, Morlanes N, Maity P, Shterk G, Mohammed OF, Gascon J. Efficient visible-light driven photothermal conversion of CO_2 to methane by nickel nanoparticles supported on barium titanate. *Adv Funct Mater* 2021;31:2008244. DOI
29. Song C, Wang Z, Yin Z, Xiao D, Ma D. Principles and applications of photothermal catalysis. *Chem Catal* 2022;2:52-83. DOI
30. Li Y, Xue J, Shen Q, et al. Construction of a ternary spatial junction in yolk–shell nanoreactor for efficient photo-thermal catalytic hydrogen generation. *Chem Eng J* 2021;423:130188. DOI
31. Li X, Zhao S, Duan X, et al. Coupling hydrothermal and photothermal single-atom catalysis toward excellent water splitting to hydrogen. *Appl Catal B Environ* 2021;283:119660. DOI
32. Gao M, Zhu L, Peh CK, Ho GW. Solar absorber material and system designs for photothermal water vaporization towards clean water and energy production. *Energy Environ Sci* 2019;12:841-64. DOI
33. Zhang T, Meng F, Gao M, et al. Multi-interfacial catalyst with spatially defined redox reactions for enhanced pure water photothermal hydrogen production. *EcoMat* 2021:3. DOI
34. Liu H, Shi L, Zhang Q, et al. Photothermal catalysts for hydrogenation reactions. *Chem Commun (Camb)* 2021;57:1279-94. DOI PubMed
35. Zhou L, Swearer DF, Zhang C, et al. Quantifying hot carrier and thermal contributions in plasmonic photocatalysis. *Science* 2018;362:69-72. DOI
36. Ng SWL, Gao M, Lu W, Hong M, Ho GW. Selective wavelength enhanced photochemical and photothermal H_2 generation of classical oxide supported metal catalyst. *Adv Funct Mater* 2021;31:2104750. DOI
37. Zhao H, Liu P, Wu X, et al. Plasmon enhanced glucose photoreforming for arabinose and gas fuel co-production over 3DOM TiO_2-Au. *Appl Catal B Environ* 2021;291:120055. DOI
38. Wegmann M, Watson L, Hendry A. XPS analysis of submicrometer barium titanate powder. *J Am Ceram Soc* 2004;87:371-7. DOI
39. Cai J, Cao A, Huang J, et al. Understanding oxygen vacancies in disorder-engineered surface and subsurface of $CaTiO_3$ nanosheets on

photocatalytic hydrogen evolution. *Appl Catal B Environ* 2020;267:118378. DOI

40. Zhu C, Wang AL, Xiao W, et al. In situ grown epitaxial heterojunction exhibits high-performance electrocatalytic water splitting. *Adv Mater* 2018;30:e1705516. DOI PubMed
41. Chang Y, Yu K, Zhang C, et al. Ternary CdS/Au/3DOM-$SrTiO_3$ composites with synergistic enhancement for hydrogen production from visible-light photocatalytic water splitting. *Appl Catal B Environ* 2017;215:74-84. DOI
42. Wu X, Zhao H, Khan MA, et al. Sunlight-driven biomass photorefinery for coproduction of sustainable hydrogen and value-added biochemicals. *ACS Sustain Chem Eng* 2020;8:15772-81. DOI
43. Hao H, Zhang L, Wang W, Zeng S. Facile modification of titania with nickel sulfide and sulfate species for the photoreformation of cellulose into hydrogen. *ChemSusChem* 2018;11:2810-7. DOI PubMed